

Enhanced fog detection and free-space segmentation for car navigation

Nicolas Hautière · Jean-Philippe Tarel ·
Houssam Halmaoui · Roland Brémond ·
Didier Aubert

Received: 31 August 2010 / Revised: 30 June 2011 / Accepted: 15 November 2011
© Springer-Verlag 2011

Abstract Free-space detection is a primary task for car navigation. Unfortunately, classical approaches have difficulties in adverse weather conditions, in particular in day-time fog. In this paper, a solution is proposed thanks to a contrast restoration approach on images grabbed by an in-vehicle camera. The proposed method improves the state-of-the-art in several ways. First, the segmentation of the fog region of interest is better segmented thanks to the computation of the shortest routes maps. Second, the fog density as well as the position of the horizon line is jointly computed. Then, the method restores the contrast of the road by only assuming that the road is flat and, at the same time, detects the vertical objects. Finally, a segmentation of the connected component in front of the vehicle gives the free-space area. An experimental validation was carried out to foresee the effectiveness of the method. Different results are shown on sample images extracted from video sequences acquired from an in-vehicle camera. The proposed method is complementary to existing free-space area detection methods relying on color segmentation and stereovision.

Keywords Free-space segmentation · Autonomous navigation · Fog detection · Meteorological visibility · Horizon line

N. Hautière (✉) · J.-P. Tarel · R. Brémond · D. Aubert
Université Paris-Est, IFSTTAR, IM, LEPSIS,
58 boulevard Lefebvre, 75015 Paris, France
e-mail: nicolas.hautiere@ifsttar.fr

H. Halmaoui
UniverSud, IFSTTAR, IM, LIVIC, 14 route de la Minière,
78000 Versailles, France

1 Introduction

Free-space detection is a fundamental task for autonomous or automated vehicles, since it provides the area where the vehicle can navigate safely. In structured environments, the free-space area is mainly composed of the road surface. This area is either detected based on color [1] or texture [2] segmentations, deduced from stereovision-based obstacles detection [3] or is a combination of both approaches [4]. However, all these methods have difficulties in foggy weather. Indeed, the contrast is reduced with the distance, which hinders classical segmentation techniques assuming that the color or the texture of the road is constant, or stereovision techniques based on local correlation from working properly. To solve this problem, one may restore the contrast of the image. Classical free-space detection techniques can then be applied to the restored image.

Methods which restore the contrast of images grabbed onboard a moving vehicle under bad weather conditions are hardly encountered in the literature. Indeed, some techniques require prior information about the scene [5]. Others require dedicated hardware in order to estimate the weather conditions [6]. Some techniques rely on two images with different fog intensities and exploit the atmospheric scattering to adequately restore the contrast [7]. Techniques based on polarization can also be used to reduce haziness in the image [8]. Unfortunately, these methods require two differently filtered images of the same scene. Finally, Narasimhan and Nayar [9] proposed to restore the contrast of more complex scenes. However, the user must manually specify a location for sky region, vanishing point and an approximation of distance distribution in the image. Recently, different methods have been proposed which rely only on a single image as input and might be used onboard a moving vehicle. Hautière et al. [10] first estimate the weather conditions and approximate a

3D geometrical model of the scene, which is inferred a priori and refined during the restoration process. The method is dedicated to in-vehicle applications. Tan [11] restores image contrasts by maximizing the contrasts of the direct transmission while assuming a smooth layer of airlight. Fattal [12] estimates the transmission in hazy scenes, relying on the assumption that the transmission and surface shading are locally uncorrelated. These methods are computationally expensive: 5–7 min with a 600×400 image on a double Pentium 4 PC for Tan [11] and 35 s with a 512×512 image on a dual core processor for Fattal [12]. Based on the principle proposed in Tan [11], i.e., the inference of the atmospheric veil, He et al. [13] as well as Tarel and Hautière [14] have proposed improved algorithms; the latter [14] is fast enough to be used in real-time applications. The problem of these methods is that the depth map produced by their atmospheric veil inference may be erroneous due to the ambiguity between white objects and fog. A novel approach combining fog detection and contrast restoration is proposed in [15] which is applied to the enhancement of driver assistance systems. Finally, a contrast restoration method able to deal with the presence of heterogeneous fog is proposed in [16].

To solely detect the free-space area, we propose another approach, taking advantage of fog presence. Following an enhanced fog detection and characterization method, the contrast of the images is restored assuming a flat world. The intensity of all the objects which do not respect this assumption thus becomes null in the restored image, which leads to a very efficient segmentation of the free-space area. This segmentation method is thus inspired from contrast restoration techniques but does not constitute a real contrast restoration method. Indeed, only the road is correctly restored.

The following of this article is organized as follows. In Sect. 2, we recall a well-known model of daytime fog, which is used to detect its presence in highway images and to estimate its density. The method is described in Sect. 3 and a sensitivity analysis is carried out which leads to propose improvements of the method in Sects. 4 and 5. In Sect. 6, we explain the principle of the flat world contrast restoration method, which is dedicated to the road, and explain how it is used to properly detect the free-space area. Finally, experimental results are given in Sect. 7 and discussed in Sect. 8.

2 Modeling fog effects in images

2.1 Koschmieder's Law

The method proposed in this study is based on a physics law governing the attenuation of brightness contrast by the atmosphere. This law, derived by Koschmieder, is given by:

$$L = L_0 e^{-\beta d} + L_\infty (1 - e^{-\beta d}) \quad (1)$$

It relates the apparent luminance L of an object located at distance d to the luminance L_0 measured close to this object at a time when the atmosphere has an extinction coefficient β . L_∞ denotes the atmospheric luminance. On the basis of this equation, Duntley developed a contrast attenuation law [17], stating that a nearby object exhibiting contrast C_0 with the background will be perceived at distance d with the following contrast:

$$C = \frac{(L_0 - L_\infty)}{L_\infty} e^{-\beta d} = C_0 e^{-\beta d} \quad (2)$$

This expression serves as a base to define a standard dimension called “meteorological visibility distance” V_{met} , i.e., the greatest distance at which a black object ($C_0 = -1$) of a suitable dimension can be seen in the sky on the horizon, with the threshold contrast set to 5% [18]. It is thus a standard dimension that characterizes the opacity of a fog layer. This definition yields the following expression:

$$V_{\text{met}} = -\frac{1}{\beta} \log(0.05) \simeq \frac{3}{\beta}. \quad (3)$$

3 Fog detection and characterization

In this section, a method to compute the extinction coefficient β using a single camera behind the vehicle windshield is recalled from [19, 20].

3.1 Flat world hypothesis

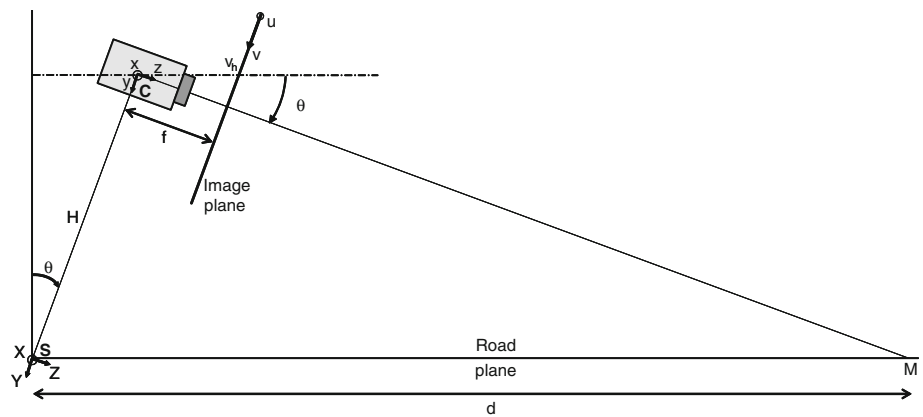
In the image plane, the position of a pixel is given by its (u, v) coordinates. The coordinates of the optical center projection in the image are designated by (u_0, v_0) . In Fig. 1, H denotes the height of the camera, θ the angle between the optical axis of the camera and a horizontal plane, and v_h the horizon line. The intrinsic parameters of the camera are its focal length f_l , and the horizontal size t_{pu} and vertical size t_{pv} of a pixel. We have also made use herein of $\alpha_u = \frac{f_l}{t_{pu}}$ and $\alpha_v = \frac{f_l}{t_{pv}}$, and have typically considered: $\alpha_u \approx \alpha_v = \alpha$. The hypothesis of a flat road is adopted, which makes it possible to associate a distance d with each line v of the image:

$$d = \frac{\lambda}{v - v_h} \text{ if } v > v_h, \text{ where } \lambda = \frac{H\alpha}{\cos\theta}. \quad (4)$$

3.2 Camera response

Let us denote f the camera response function, assumed to be linear, which models the mapping from scene luminance to image intensity by the imaging system, including optic as well as electronic parts. In a foggy scene, the intensity I of

Fig. 1 Modeling of the camera within its environment; it is located at a height of H in the (S, X, Y, Z) coordinate system relative to the scene. Its intrinsic parameters are its focal length f and pixel size t . θ is the angle between the optical axis of the camera and the horizontal. Within the image coordinate system, (u, v) designates the position of a pixel, (u_0, v_0) is the position of the optical center C and v_h is the vertical position of the horizon line



a pixel is the result of f applied to (1):

$$I = f(L) = f(L_0)e^{-\beta d} + f(L_\infty)(1 - e^{-\beta d}) = R e^{-\beta d} + A_\infty(1 - e^{-\beta d}) \tag{5}$$

where, R is the intrinsic intensity of the pixel, i.e., the intensity corresponding to the intrinsic luminance value of the corresponding scene point and A_∞ is the background sky intensity.

3.3 Recovery of fog parameters

Following a variable change from d to v based on (4), (5) thus becomes:

$$I = A_\infty + (R - A_\infty)e^{-\beta \frac{\lambda}{v-v_h}} \tag{6}$$

By twice taking the derivative of I with respect to v , one obtains the following:

$$\frac{\partial^2 I}{\partial v^2} = \beta \varphi(v) e^{-\beta \frac{\lambda}{v-v_h}} \left(\frac{\beta \lambda}{v - v_h} - 2 \right) \tag{7}$$

where, $\varphi(v) = \frac{\lambda(R-A_\infty)}{(v-v_h)^3}$. The equation $\frac{\partial^2 I}{\partial v^2} = 0$ has two solutions. The solution $\beta = 0$ is of no interest. The only useful solution is:

$$\beta = \frac{2(v_1 - v_h)}{\lambda} \tag{8}$$

where v_1 denotes the position of the inflection point of $I(v)$. Thus from v_1 , the parameter β of Koschmieder's law is obtained. Finally, thanks to v_1 , v_h and β values, the values of the other parameters of (5) are deduced through use of I_1 and $\frac{\partial I}{\partial v}|_{v=v_1}$, which are respectively the values of the function I and its derivative in $v = v_1$:

$$\begin{cases} R = I_1 - (e^2 - 1) \frac{(v_1-v_h)}{2} \frac{\partial I}{\partial v}|_{v=v_1} \\ A_\infty = I_1 + \frac{(v_1-v_h)}{2} \frac{\partial I}{\partial v}|_{v=v_1} \end{cases} \tag{9}$$

where, R is the intrinsic intensity of the road surface.

To originally implement this method, we measure the median intensity on each line of a vertical band in the image.

As this band should only take into account a homogeneous area and the sky, we identify a region within the image which displays minimal line-to-line gradient variation when crossed from bottom to top using a recursive region growing algorithm. If such a region can be found, fog is detected. A vertical band is then selected in the segmented area. Thus, we obtain the vertical variation of the intensity in the image, and deduce β by computing the maximum of the first derivative of this profile.

3.4 Method discussion

The fog detection method presented in the previous paragraph has two major limitations which are now discussed.

3.4.1 Segmentation of the region of interest

First, the method is sensitive to the presence of obstacles such as a preceding vehicle which might prevent the region growing algorithm to cross the image from bottom to top. However, as long as a vertical path exists in the image, the region growing is able to circumvent the obstacles, which makes it possible to detect fog presence. A temporal filter can also be used if fog is temporary not detected. An example of temporal filter dedicated to our problem is proposed in [21].

Another limitation is related to the method of segmentation of the region of interest (ROI). As said previously, this method identifies a region within the image which displays minimal line-to-line gradient variation when crossed from bottom to top, using a region growing algorithm which aims at segmenting part of the road and the sky regions. In particular, a hard threshold is used to set the maximum allowed line-to-line gradient. This threshold is difficult to set depending of the image. Moreover, the method fails in case of highly textured road surfaces. Then, in case of a strong transition between the road and the sky, the region growing is not able to segment the sky. Finally, the criterion to stop the region growing algorithm is too strong. Indeed, the image must be crossed from bottom to top, which is not possible in case

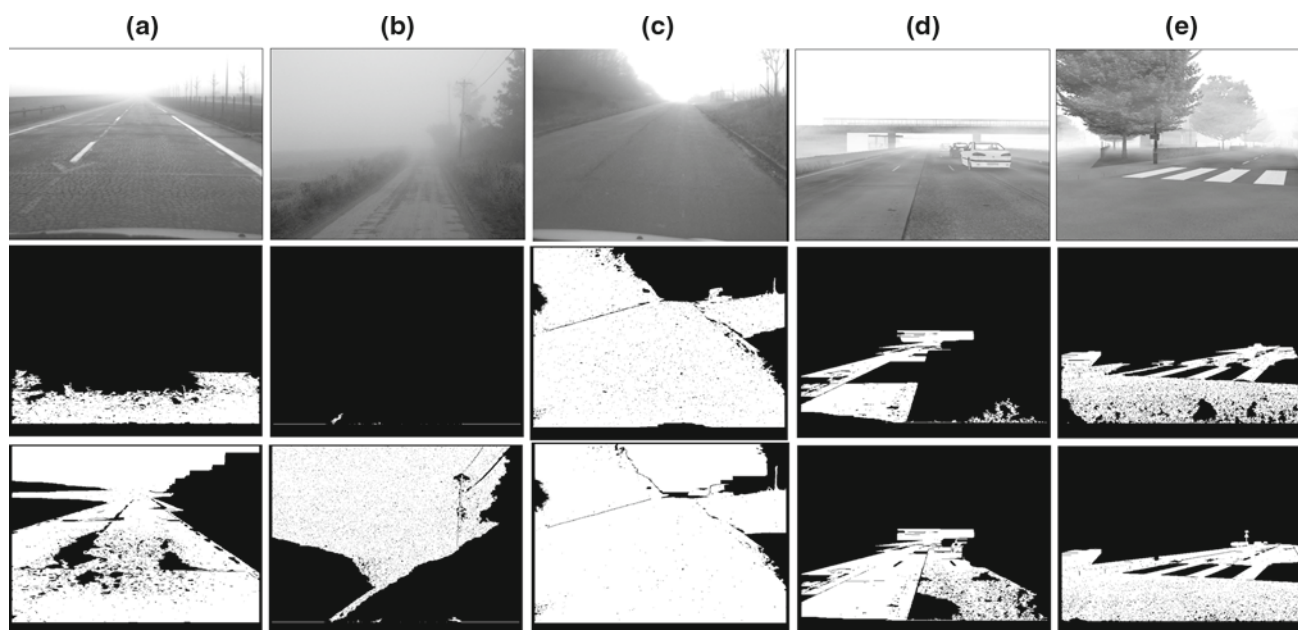


Fig. 2 Challenging images with which the original ROI segmentation method proposed in [19] gives poor results. The original images are shown in the first row. The second and third row show the results, respectively, obtained with $\Delta_s = 2$ and $\Delta_s = 3$

of road signs or a bridge above the road. Finally, the recursive implementation of the algorithm may be problematic for some hardware architectures.

In Fig. 2, some challenging images are shown with results obtained using the original ROI segmentation method which gives poor results. The original images are shown in the first row. The second and third row show the results, respectively, obtained with $\Delta_s = 2$ and $\Delta_s = 3$, where Δ_s denotes the local gradient threshold. The difference of results with very close thresholds illustrate the sensitivity of this method with respect to this local threshold. Fig. 2a, b illustrates the difficulty to process textured road surfaces. Figure 2c illustrates the difficulty to process scenes with very strong transitions between road and sky. Finally, Fig. 2d, e, issued from the FRIDA database [16], illustrate the difficulty to process scene with objects above the road surface (buildings, trees, bridge).

3.4.2 Pitch angle sensitivity

Second, the proposed measurement process is sensitive to variations of orientation of the vehicle with respect to the road surface. It is not too much sensitive to variations of roll angle thanks to the use of a measurement bandwidth, contrary to a change of pitch angle. Indeed, the estimation of V_{met} is correct if the position v_1 of the inflection point as well as the position v_h of the horizon line are correct.

Let us study the influence of an estimation error δ on the difference between these two positions. The error S between the estimated meteorological visibility distance \tilde{V}_{met} and the

actual meteorological visibility distance V_{met} is expressed with respect to δ by:

$$\begin{aligned}
 S &= V_{\text{met}} - \tilde{V}_{\text{met}} \\
 &= V_{\text{met}} - \frac{3\lambda}{2} \frac{1}{v_1 - v_h + \delta} \\
 &= V_{\text{met}} \left[1 - \frac{1}{1 + \frac{2\delta V_{\text{met}}}{3\lambda}} \right]
 \end{aligned} \tag{10}$$

The curves in Fig. 3 show the error for values of δ ranging from -4 to $+4$ pixels. One clear result is that underestimating δ is more penalizing than overestimating it. To have stable measurements, we may choose to set the horizon line above its theoretical position.

However, estimating the position of the horizon line is a difficult problem. It can be estimated by means of the pitching of the vehicle when an inertial sensor is available, but is generally estimated by an additional image processing. This type of processing seeks to intersect the vanishing lines in the image, see [22,23] for instance. However, under foggy weather, the vanishing lines are only visible close to the vehicle. It is thus necessary to extrapolate the position of the horizon line through the fog. Consequently, this kind of process is prone to a significant standard deviation and, so far, using the a priori sensor calibration was a better option.

In this section, two major limitations of the method published in [19,20] have been highlighted. The novel proposals described in the next two sections aim at solving these issues.

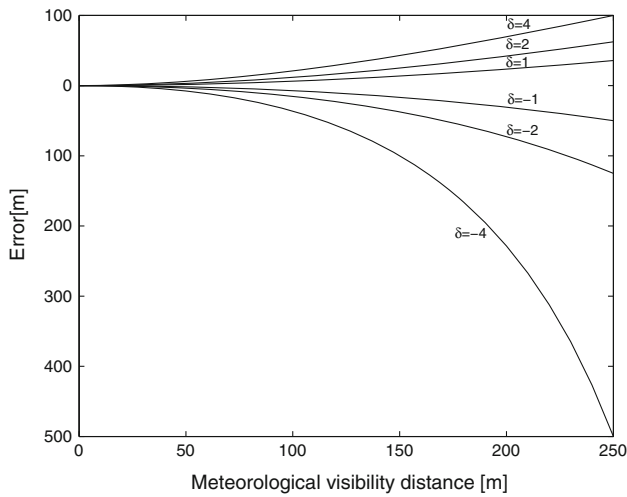


Fig. 3 Method sensitivity with respect to the estimation error δ between v_1 and v_h . Used camera parameter: $\lambda = 1000$

4 Segmentation of fog ROI based on geodesic maps

In this section, a novel approach for the fog ROI segmentation is presented to circumvent the previous limitations, thanks to the use of geodesic maps.

4.1 Optimal path computation in gray-level images

Following the original idea that the fog ROI should display a minimal line-to-line gradient [19], an analogy with optimal path computation methods can be made. Assimilating an image with a graph, Dijkstra’s algorithm [24] allows computing the shortest path but the complexity of the algorithm $O(n^2)$ is problematic for large images. More efficient approaches exist, making use of heuristics like the A^* algorithm [25] but the complexity is still $O(n \log n)$ for computing one single source shortest path. In our case, it is problematic since the goal is to compute the shortest routes between sets of nodes. The weighted distance transform on curved space (WDTACS) proposed in [26] aims at computing the shortest routes between sets on gray-level images.

The WDTACS uses piecewise Euclidian local distance computed with Pythagora’s theorem from the horizontal displacement and the height difference. It is also referred as the efficient geodesic distance transform [27] (see also [28]). Its principle is presented in Fig. 4.

The route algorithm using WDTACS requires two distance maps $\mathcal{F}_a^*(x)$ and $\mathcal{F}_b^*(x)$. The route endpoint a (respectively, b) is the feature from which all distances are computed. From the distance maps, a route distance image is computed by a simple addition:

$$\mathcal{D}_R(x) = \mathcal{F}_a^*(x) + \mathcal{F}_b^*(x) \tag{11}$$

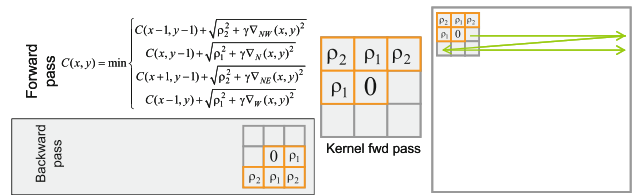


Fig. 4 Efficient geodesic distance transform [27]. Usually, $\rho_1 = 1$ and $\rho_2 = \sqrt{2}$

The value $\mathcal{D}_R(x)$ is the distance between the route end-points along the shortest path passing through point x . Consequently, the points with a minimal route distance value form the desired route:

$$\mathcal{R}(a, b) = \{x | \mathcal{D}_R(x) = \min_x \mathcal{D}_R(x)\} \tag{12}$$

This idea can be generalized for a general route between sets. The route between sets is found by computing the distance maps $\mathcal{F}_A^*(x)$ and $\mathcal{F}_B^*(x)$, where A and B are the point sets between which we want to find an optimal route. The distance map $\mathcal{R}(A, B)$ is deduced as well.

4.2 Novel fog ROI segmentation approach

The optimal route computation approach detailed in the previous section may be adapted to segment fog region of interest. The sets A and B have to be correctly chosen. We thus make two minimal assumptions. First, we assume that the road is at the bottom of the image, i.e., in front of the car. A is the lowest line in the image belonging to the road surface. Second, we assume that the sky area is among the brightest pixels of the image above an *a priori* estimation of the horizon line. B is thus made of the brightest pixels of the image. Once the route map is obtained, a segmentation of the minimum route $\tilde{\mathcal{R}}(A, B)$ is performed starting from the bottom of the image and stopping the highest possible in the image using a tolerance τ parameter applied to (12):

$$\tilde{\mathcal{R}}(A, B) = \{x | \mathcal{D}_R(x) \leq (1 + \tau) \min_x \mathcal{D}_R(x)\} \tag{13}$$

Finally, the method has no local parameter anymore. Instead, we use two global parameters: γ represents the relative weight of the gradient with respect to the Euclidian distance in the geodesic transform (cf. Fig. 4) and τ governs the final extraction of the minimum route. Then, the segmentation is successful if the segmentation region goes above the theoretical position of the horizon line position. The process is illustrated in Fig. 5 on a challenging road scene. Fig. 5b shows the origin and destination set points. Figure 5c, d, show, respectively, $\mathcal{F}_A^*(x)$ and $\mathcal{F}_B^*(x)$ distance maps. Figure 5e shows the final route map. Figure 5f shows the segmented fog ROI overlaid on the original image.

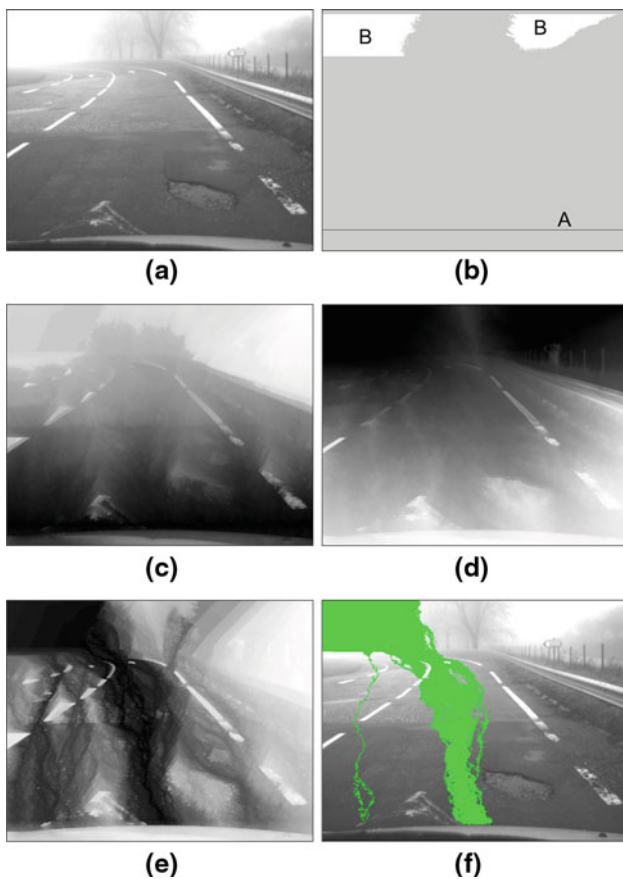


Fig. 5 Fog ROI segmentation based on WDTOCS transform: **a** original image; **b** origin (*A*) and destination (*B*) set points; **c** $\mathcal{F}_A^*(x)$ distance map; **d** $\mathcal{F}_B^*(x)$ distance map; **e** $\mathcal{R}(A, B)$ route map; **f** final segmented ROI overlaid on the original image. In the distance maps, the distance is mapped linearly into gray levels

5 Horizon line position

In Sect. 3.4.2, the sensitivity of the fog density estimation algorithm to the horizon line position has been highlighted. In this section, a new estimation method is proposed.

5.1 Joint estimation of the horizon line position

By taking the derivative of I with respect to v one more time, we obtain the following:

$$\frac{\partial^3 I}{\partial v^3}(v) = \frac{\beta\lambda(R - A_\infty)}{(v - v_h)^6} (6v[v - (\beta\lambda + 2v_h)] + \dots + 6v_h[\beta\lambda + v_h] + \beta^2\lambda^2)e^{-\frac{\beta\lambda}{v-v_h}} \quad (14)$$

Thus, the derivative of Koschmieder’s law owns two inflection points whose locations are denoted v_2 and v_3 :

$$\begin{cases} v_2 = v_h + \frac{\beta\lambda(3-\sqrt{3})}{6} \\ v_3 = v_h + \frac{\beta\lambda(3+\sqrt{3})}{6} \end{cases} \quad (15)$$

Thanks to (8) and (15), the position of the horizon line v_h can be computed for each inflection point of the derivative:

$$\begin{cases} v_h = (1 - \sqrt{3})v_1 + \sqrt{3}v_2 \\ v_h = (1 + \sqrt{3})v_1 - \sqrt{3}v_3 \end{cases} \quad (16)$$

For each inflection point of the derivative, we deduce an estimation of β :

$$\begin{cases} \beta = \frac{2\sqrt{3}}{\lambda}(v_1 - v_2) \\ \beta = \frac{2\sqrt{3}}{\lambda}(v_3 - v_1). \end{cases} \quad (17)$$

5.2 Accurate estimate

Generally, the estimation of the position the most important inflection point of a signal is made by looking for the location where the first derivative is maximum. Consequently, v_1 is obtained as the location where the first derivative of I is maximum. v_2 is obtained by looking at the location of the maximum of the second derivative of I between the top of the image and v_1 . v_3 is obtained by looking at the location of the maximum of the second derivative of between the bottom of the image and v_1 .

We are thus able to estimate the extinction coefficient of the atmosphere as soon as we are able to detect the inflection point of the intensity curve as well as to estimate the position of one of its inflection points, figured out in Fig. 6. In this way, we are able to simultaneously estimate the position of the horizon line. From a practical point of view, the results using v_2 , the inflection point between the sky and v_1 , are more accurate since they are less sensitive to the texture of the road surface. However, both estimators might be combined by giving a lower weight to the measurements based on v_3 .

Whatever the technique used to estimate the vertical intensity profile I , the obtained profile is noisy. It is thus necessary to smooth the profile before extracting the positions of the different inflection points v_1 , v_2 and v_3 . Usually, the profile is over-sampled ten times so as to have a sampling uncertainty smaller than one-tenth of a pixel. The problem is that the application of a smoothing filter (Gaussian for instance) on the profile, even if it reduces the noise, is likely to bias the position of the inflection points, as shown for v_1 in Fig. 7. To have correct results, it is thus necessary to correct this bias. This correction is performed in two steps.

The first step consists in smoothing the signal with two filters having different scales, typically $s_m = 15$ pixels and $s_M = 30$ pixels. We denote $v_{i,m}$ and $v_{i,M}$ the estimated position of one of the inflection point ($i = 1$ or 2). The extrapolated position of the inflection point at zero scale is given by:

$$v_i = \frac{s_M \times v_{i,m} - s_m \times v_{i,M}}{s_M - s_m} \quad (18)$$

The values of β , v_h , A_∞ and R are deduced according to the previous equations (9), (16) and (17).

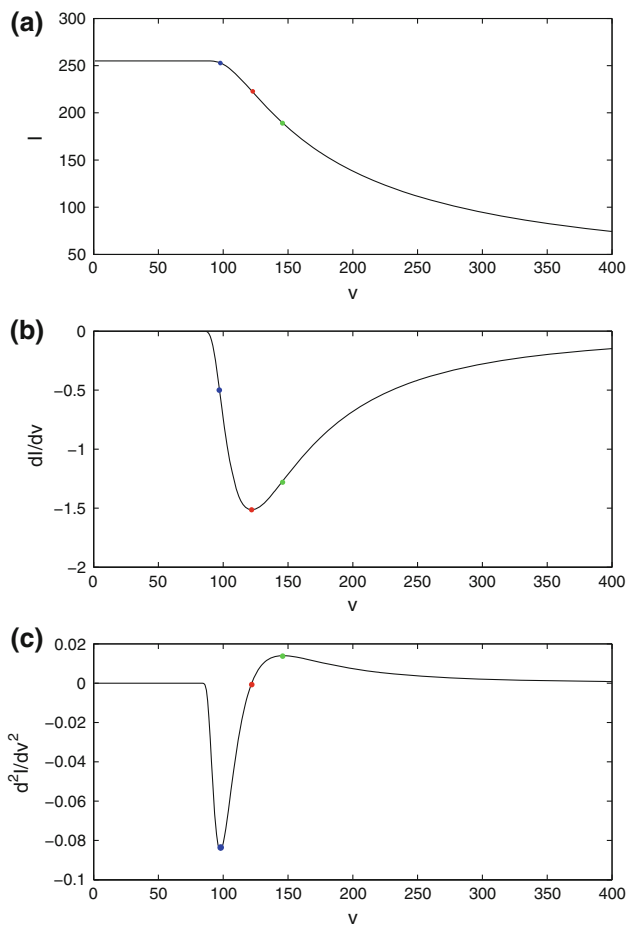


Fig. 6 Points of interest on (a) Koschmieder’s law and its (b) first and (c) second derivative. The *middle point* denotes the inflection point v_1 . The *left* and the *right* points denote the inflection points v_2 and v_3 , respectively

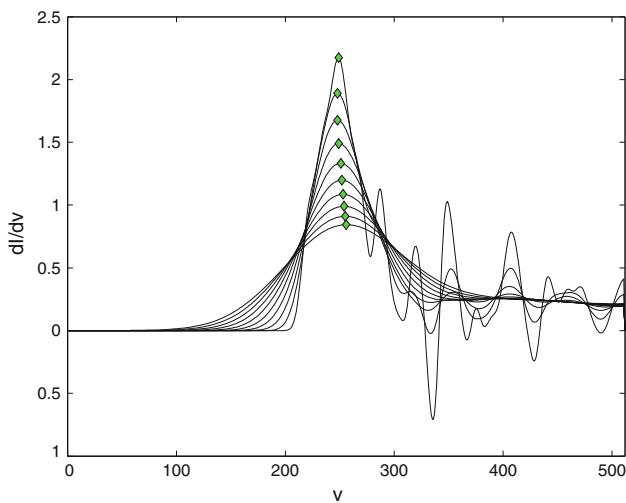


Fig. 7 Derivative of the luminance curve I for different smoothing levels. The location of the inflection point v_1 is marked with a *diamond*. The displacement of its location with respect to the smoothing level is obvious

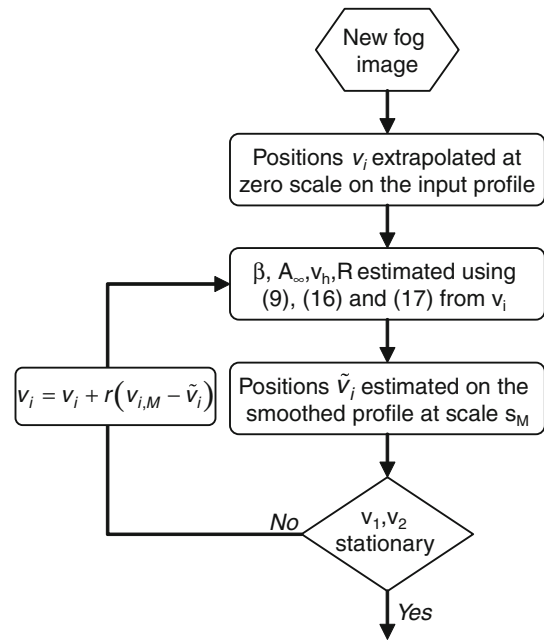


Fig. 8 Diagram of the algorithm used to accurately estimate the positions of the inflection points

The second step consists in reconstructing the intensity profile based on the values of β , v_h , A_∞ and R estimated thanks to the first step. Then, we apply a smoothing of scale s_M on the reconstructed profile and estimate, from the smoothed profile, the positions of the inflection points \tilde{v}_1 and \tilde{v}_2 . The values v_1 and v_2 are then updated, taking into account the residual bias by adding the term $r(v_{i,M} - \tilde{v}_i)$, $i = 1$ or 2 , where r denotes a ratio inferior to 1, typically 0.8. The second step is iterated until the sum of distances between the successive \tilde{v}_i and \tilde{v}_i is small enough. The number of possible iterations is limited. The algorithm is schematized on Fig. 8.

6 Free-space detection method

6.1 Restoration principle

In this section, we describe a simple method to restore scene contrast from a foggy image. Let us consider a pixel with known depth d . Its intensity I is given by (5). (A_∞, β) characterizes the weather condition and are previously estimated. Consequently, R can be estimated directly for all scene points from (5):

$$R = Ie^{\beta d} + A_\infty(1 - e^{\beta d}) \tag{19}$$

This equation means that an object exhibiting a contrast C in the original image will have the following contrast C_r with

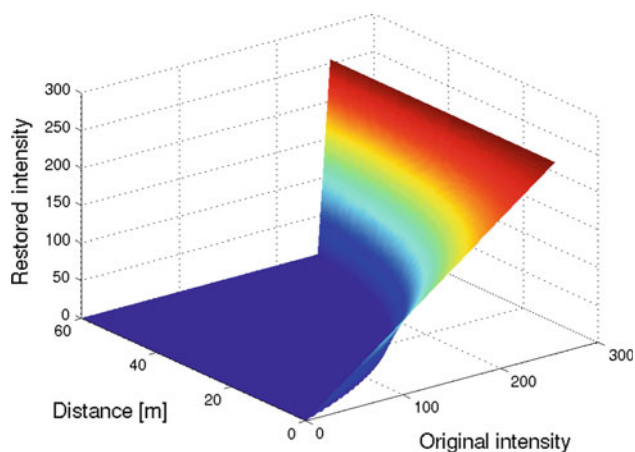


Fig. 9 3D plot of the corrected contrast restoration function (21) for $\beta = 0.05$ and $A_\infty = 255$. The object intensity may become null after contrast restoration

respect to the background sky in the restored image:

$$C_r = \frac{(R - A_\infty)}{A_\infty} = \frac{(I - A_\infty)}{A_\infty} e^{\beta d} = C e^{\beta d} \quad (20)$$

We thus have a method which restores the contrast exponentially with respect to the depth. Unfortunately, R is negative for some values of (I, d) . In such cases, we clip these values to 0. The restoration equation becomes finally:

$$R = \max \left[0, I e^{\beta d} + A_\infty (1 - e^{\beta d}) \right] \quad (21)$$

This function was plotted for a certain range of (I, d) values in Fig. 9. To properly restore the scene contrast, the remaining problem is to estimate the depth d at each pixel.

6.2 Flat world restoration

Based on (21), a 3D model of the road scene is necessary to restore the contrast accurately. As a first step, we propose to use a quite opposite scheme, which only assumes that the road is flat. The distance of a pixel in the image is thus assumed given by (4). Large distances are clipped using a parameter c . The distance d_c of a pixel $P(i, j)$ is thus expressed by:

$$d_c(i \in [0, N[, j \in [0, M[) = \begin{cases} \frac{\lambda}{j-v_h} & \text{if } M > j > c \\ \frac{\lambda}{c-v_h} & \text{if } 0 \leq j \leq c \end{cases} \quad (22)$$

where, $N \times M$ denotes the size of the image. c serves to set the maximum distance for the contrast restoration. It makes sense to set the position of this clipping plane at the meteorological visibility distance. Indeed, no pixel has a contrast above 5% beyond V_{met} . Consequently, the structure of the scene is unknown beyond this distance. Using (3) and (8), we thus set:

$$c = \frac{(2v_1 + v_h)}{3} \quad (23)$$

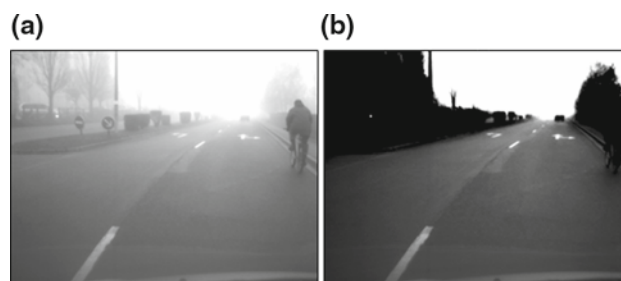


Fig. 10 Sample result of flat world restoration. The intensity of vertical objects becomes null in the restored image: **a** original image; **b** result

Using (22) in (21), the contrast of objects belonging to the road plane is correctly restored.

6.3 Free-space segmentation

Conversely, as soon as they are darker than the sky, i.e., $I < A_\infty$, the contrast of vertical objects of the scene (other vehicles, trees, etc.) is falsely restored since their distance in the scene is largely overestimated. Consequently, according to (21), their intensity becomes null in the restored image thanks to the exponential formula, like in Fig. 10b. This is an inconvenience of this method, which was mitigated in [29] by underestimating the value of the horizon line. However, this inconvenient can be turned into our advantage. Thus, by detecting the pixels whose intensity is null after contrast restoration, we easily segment the vertical objects and then segment the free-space area accordingly by looking for the biggest connected component in front of the vehicle. To improve the results of this last step, a morphological opening of the connected component may be performed.

7 Experimental validation

In the previous sections, three contributions have been presented: a fog ROI segmentation method, a process to jointly estimate the horizon line and the fog density and a method to segment the free-space navigation area. In this section, experimental results are presented to illustrate the relevance of each of these contributions.

7.1 Fog ROI segmentation

The fog ROI segmentation has been tested on actual fog images as well as on synthetic images from the FRIDA database [16]. From a qualitative viewpoint, the proposed method appears to be very effective. The sensitivity to the internal parameters of the method is limited. The limitations of the original segmentation which were outlined in Sect. 3.4 were circumvented. The local gradient parameter was replaced by



Fig. 11 Sample results of fog ROI segmentations obtained with the novel method on challenging images including the ones used in Fig. 2. The parameters of the method $\gamma = 10$ and $\tau = 5\%$. The original images

are shown in the *first* and *third* rows. Results are shown in the *third* and *fourth* row

the γ internal parameter of the geodesic image transform. Consequently, the texture of the road does not block the method anymore. The criteria to stop the segmentation is not so constraining. The abrupt transition between the road and the surface is not problematic anymore, thanks to a rough segmentation of the sky area. Finally, the complexity of the algorithm is much reduced and is quasi-linear. No recursive scheme is used anymore which may ease the implementation of the algorithm on hardware architectures.

To show qualitatively the effectiveness of our method, different experimental results obtained with the same parameters ($\gamma = 10$ and $\tau = 5\%$) are shown in Fig. 11. The images from Fig. 2, where the original method was inoperative, are used as well as other challenging scenes that the original method was already able to cope with. As one can see, the segmented ROIs meet the constraints of Koschmieder's law and allow the computation of the fog density as well as of the actual position of the horizon line.

7.2 Joint fog density and horizon line estimation

Sample results of the joint meteorological visibility distance and horizon line position estimation are shown in Fig. 12 on synthetic images as well as on an real images. In these pic-

tures, the overlaid area denotes the limits of the fog ROI. The vertical noisy profile denotes the median gray level profile measured on each line of the fog ROI. This profile instantiates Koschmieder's law. The vertical smooth profile denotes the reconstructed profile. The horizontal black line denotes the estimated position of the horizon line. The horizontal purple line denotes the estimated meteorological visibility distance. On synthetic images such as Fig. 12a, the accuracy is good for low visibilities (<150 m). For higher visibilities, the accuracy might be smaller, because of the angular size of the pixels and of the presence of objects in front of the background sky. Indeed, the road surface represented by a single pixel is hyperbolic with respect to the distance [19]. Consequently, the accuracy of the estimation is necessarily reduced when the visibility increases. On sensor images such as Fig. 12b, we can only comment that the location of the different lines seems adequate, since the ground truth is not available.

7.3 Free-space detection

A way to assess the joint fog density and horizon line estimation process is to assess its ability to segment the free-space area. Using the proposed method, we obtain the results shown in Fig. 14. From a qualitative point of view, we get good

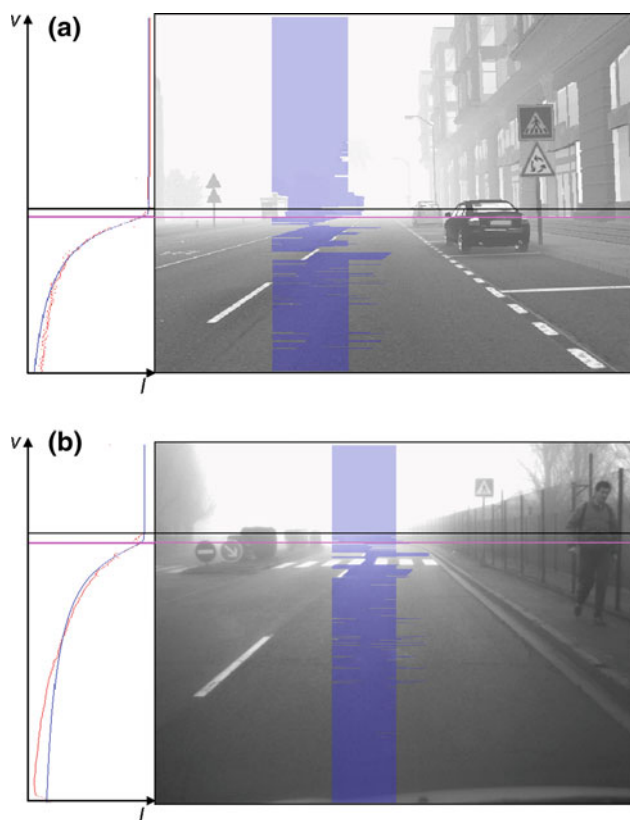


Fig. 12 Sample results of joint meteorological visibility distance and horizon line position estimation on a **(a)** synthetic image ($V_{\text{met}} = 91.6$ m and $v_h = 257$): $V_{\text{met}}^{\text{est}} = 92$ m and $v_h^{\text{est}} = 260$; **(b)** an actual image: $V_{\text{met}}^{\text{est}} = 87$ m and $v_h^{\text{est}} = 145$. The *vertical noisy profile* denotes the median gray level profile measured on each line of the fog ROI. The *vertical smooth profile* denotes the reconstructed profile. The *horizontal upper line* denotes the estimated position of the horizon line. The *horizontal lower line* denotes the estimated meteorological visibility distance

results, even if some minor improvements could be made on the segmentation of curbs, sidewalks and very bright objects, i.e., objects whose intensity is equal to or higher than the sky intensity. The quality of these results seems comparable to color-based or stereovision approaches.

To assess quantitatively this free-space segmentation, we have used a receiver operating characteristic (ROC) curve. The larger the area under the ROC curve, the better the extractor. In our case, this curve is obtained by plotting the true positive rate (TPR) versus the false positive rate (FPR) for different values of a corrective coefficient ρ applied to the meteorological visibility distance V_{met} found automatically by the algorithm. We do not change the other parameters of the algorithm, in particular the position of the horizon line. In this aim, we have extracted manually the free-space region (ground truth) on different images from a small database of 15 images. The TPR is the rate of pixels which belong to the free-space region and is detected as part of this region

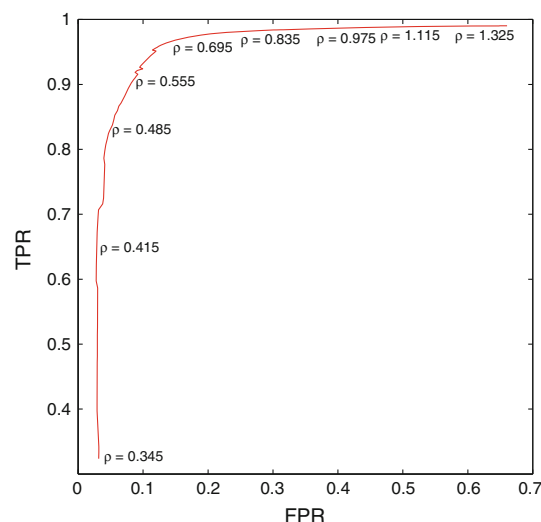


Fig. 13 ROC curve of the free-space detection obtained on a 15 images database. The true positive rate (TPR) is plotted versus the false positive rate (FPR) for different values of the corrective coefficient ρ applied to the meteorological visibility distance V_{met}

by the algorithm. The FPR is the rate of pixels which do not belong to the free-space region and is detected as part of this region by the algorithm. The ROC curve is plotted in Fig. 13. When segmenting the ground truth, an ambiguity was found in the definition of the free-space area. Is it the road surface only or does it also include other flat areas like the sidewalks where vehicles can also evolve? We chose the most restrictive definition of the free-space, i.e., the road surface only. The parameters found by the automatic process ($\rho = 1$) lead to a TPR close to 1 and a FPR close to 0.4. It means that there are some false detection. This is especially the case on the sidewalks and curbs which are detected as a part of the free-space area by the algorithm (see Fig. 14c for example), which was expected due to the definition chosen for the free-space area. A corrective coefficient ($\rho < 1$) reduces the FPR. Indeed, by reducing the estimated meteorological visibility distance, the contrast restoration is stronger, so that objects like curbs and sidewalks are also detected as obstacles. $\rho = 0.6$ leads to TPR=95% and FPR=10% on our database. As one can see, the algorithm is able to perform a quite accurate segmentation.

7.4 Discussion

The proposed method allows to obtain good results, even if minor improvements could be made on the segmentation of sidewalks and very bright objects, i.e., the objects whose intensity is higher than the sky intensity A_∞ . The quality of these results seems comparable with color-based or stereovision approaches. The good point in our method is that we only use one gray-level image. However, it only works in

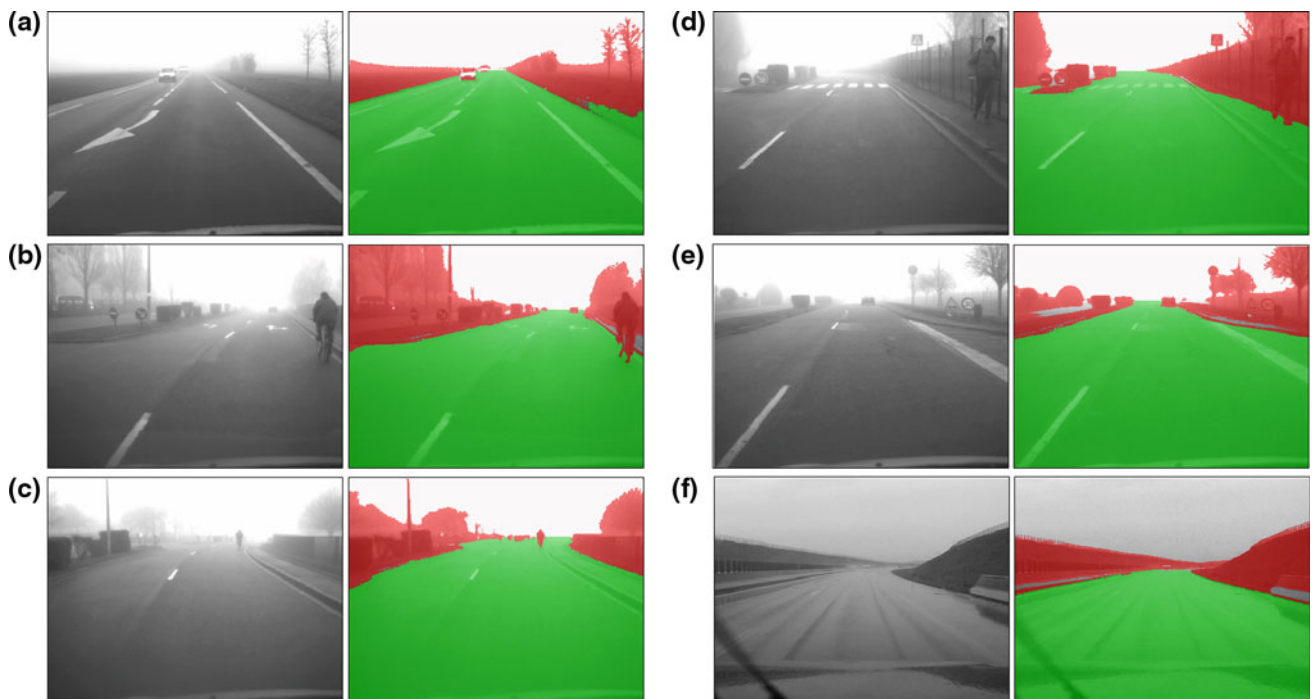


Fig. 14 Free-space detection of the road scene. *First and third columns* original images. *Second and fourth columns* results of vertical objects segmentation are overlaid on the original images. The figure at the *bottom-right* shows a test using a rainy weather image (in this case, β is set manually)

daytime foggy weather. The classical methods and the proposed one are thus complementary. Of course, the proposed method has the limitations of all monocular methods, i.e., it is restricted to flat world scenes. On the one hand, the fog detection method is able to estimate both the fog density and the position of the horizon line. Even if the novel fog ROI segmentation improves drastically the original method, the method is still sensitive to the presence of big objects in front of the vehicle (see [19] for more details). On the other hand, the segmentation method is not too sensitive to the inhomogeneity of fog and can be applied to other weather conditions such as rainy weather. A sample of rainy weather image is shown in Fig. 14f.

From a hardware point of view, the computation of the fog density alone takes less than 40 ms in C++ using a 2.4-GHz Intel Core 2 Duo PC on 1/4 PAL images. On the same hardware platform, the free-space detection takes less than 20 ms. However, the joint estimation process of the meteorological visibility and the horizon line is iterative. Its computation time depends on the number of iterations. Each iteration takes 20 ms. Usually, we limit the algorithm to a maximum of 10 iterations, i.e., a maximum of 260 ms, before skipping the image in case of no convergence and to process a new one. The algorithm has still to be optimized to be operated at frame rate.

8 Conclusion

A solution was proposed to detect the free-space area in foggy road scenes thanks to a contrast restoration approach. First, the method estimates simultaneously the density of fog and the position of the horizon line in the image, which improves drastically the state-of-the-art in this area. A highly effective fog ROI segmentation method based on geodesic maps computation is proposed as well as a novel joint fog density and horizon line estimation process. Thanks to a simple contrast restoration method, the proposed method is then able to restore the contrast of the road and at the same time to segment the vertical objects. Indeed, these objects are falsely restored and in this way easily segmented. An experimental validation allows figuring out the potential of the method. Results on sample images extracted from video sequences acquired from an in-vehicle camera are shown and discussed. In the future, we would like to integrate these works in prototypes and test intensively the method, so as to identify some eventual new problems which could appear.

Acknowledgments This work is partly funded by the ANR (French National Research Agency) within the ICADAC project (6866C0210).

References

1. Crisman, J., Thorpe, C.: Unscarf: A color vision system for the detection of unstructured roads. In: IEEE International Conference on Robotics and Automation, Sacramento, USA, pp. 2496–2501 (1991)
2. Zhang, J., Nagel, H.: Texture-based segmentation of road images. In: IEEE Intelligent Vehicles Symposium, pp. 260–265 (1994)
3. Broggi, A., Caraffi, C., Fedriga, R., Grisleri P.: Obstacle detection with stereo vision for off-road vehicle navigation. In: IEEE Workshop on Machine Vision for Intelligent Vehicles, San Diego, USA, pp. 65–73 (2005)
4. Soquet, N., Aubert, D., Hautière, N.: Road segmentation supervised by an extended v -disparity algorithm for autonomous navigation. In: IEEE Intelligent Vehicles Symposium, Istanbul, Turkey, pp. 160–165 (2007)
5. Oakley, J.P., Satherley, B.L.: Improving image quality in poor visibility conditions using a physical model for contrast degradation. In: IEEE Transactions on Image Processing, vol. 7, pp. 167–179 (1998)
6. Yitzhaky, Y., Dror, I., Kopeika, N.: Restoration of atmospherically blurred images according to weather-predicted atmospheric modulation transfer function. *Optic. Eng.* **36**, 3064–3072 (1997)
7. Narasimhan, S.G., Nayar, S.K.: Contrast restoration of weather degraded images. *IEEE Trans. Pattern Anal. Mach. Intell.* **25**(6), 713–724 (2003)
8. Schechner, Y., Narasimhan, S., Nayar, S.: Polarization-based vision through haze. *Appl. Optic. Special Issue* **42**(3), 511–525 (2003)
9. Narashiman, S.G., Nayar, S.K.: Interactive deweathering of an image using physical model. In: IEEE Workshop on Color and Photometric Methods in Computer Vision (2003)
10. Hautière, N., Tarel, J.-P., Aubert, D.: Towards fog-free in-vehicle vision systems through contrast restoration. In: IEEE Conference on Computer Vision and Pattern Recognition, Minneapolis, Minnesota, USA, pp. 1–8 (2007)
11. Tan, R.T.: Visibility in bad weather from a single image. In: IEEE Conference on Computer Vision and Pattern Recognition, Anchorage, Alaska, USA, pp. 1–8 (2008)
12. Fattal, R.: Single image dehazing. *ACM Trans. Graph.* **27**(3), 1–9 (2008)
13. He, K., Sun, J., Tang, X.: Single image haze removal using dark channel prior. In: IEEE Conference on Computer Vision and Pattern Recognition, Miami, Florida, USA, pp. 1956–1963 (2009)
14. Tarel, J.-P., Hautière, N.: Fast visibility restoration from a single color or gray level image. In: IEEE International Conference on Computer Vision, Kyoto, Japan, pp. 2201–2208 (2009)
15. Hautière, N., Tarel, J.-P., Aubert, D.: Mitigation of visibility loss for advanced camera based driver assistances. *IEEE Trans. Intell. Transport. Syst.* **11**(2), 474–484 (2010)
16. Tarel, J.-P., Hautière, N., Cord, A., Gruyer, D., Halmaoui, H.: Improved visibility of road scene images under heterogeneous fog. In: IEEE Intelligent Vehicles Symposium, San Diego, Californie, USA, pp. 478–485 (2010)
17. Middleton, W.: Vision through the atmosphere. University of Toronto Press, Toronto (1952)
18. Commission Internationale de l'Éclairage.: International lighting vocabulary, no. 17.4 (1987)
19. Hautière, N., Tarel, J.-P., Lavenant, J., Aubert, D.: Automatic fog detection and estimation of visibility distance through use of an onboard camera. *Mach. Vis. Appl. J.* **17**(1), 8–20 (2006)
20. Lavenant, J., Tarel, J., Aubert, D.: Procédé de détermination de la distance de visibilité et procédé de détermination de la présence d'un brouillard, French Patent 0201822, LCPC/INRETS (2002)
21. Hiramatsu, T., Ogawa, T., Haseyama, M.: A kalman filter-based method for restoration of images obtained by an in-vehicle camera in foggy conditions. *IEICE Trans. Fundamentals Electron. Commun. Comput. Sci.* **E92.A**(2), 577–584 (2009)
22. Tarel, J.-P., Aubert, D., Guichard, F.: Tracking occluded lane-markings for lateral vehicle guidance. In: Recent Advances in Signal Processing and Communications, World Scientific and Engineering Society Press, Japan, pp. 154–159 (1999)
23. Kong, H., Audibert, J.-Y., Ponce, J.: Vanishing point detection for road detection. In: IEEE Conference on Computer Vision and Pattern Recognition, Miami, Florida, USA, pp. 96–103 (2009)
24. Dijkstra, E.W.: A note on two problems in connection with graphs. *Numerische Math.* **1**, 269–271 (1959)
25. Hart, P.E., Nilsson, N.J., Raphael, B.: A formal basis for the heuristic determination of minimum cost paths. *IEEE Trans. Syst. Sci. Cybernet.* **4**(2), 100–107 (1968)
26. Ikonen, L., Toivanen, P.: Shortest routes between sets on gray-level surfaces. *Pattern Recogn. Imag. Anal.* **15**(1), 195–198 (2005)
27. Crisiminisi, A., Sharp, T., Blake, A.: GeOS: Geodesic image segmentation. In: European Conference on Computer Vision, Marseille, France (2008)
28. Brémont, R., Jeulin, D., Gateau, P., Jarrin, J., Serpe, G.: Estimation of the transport properties of polymer composites by geodesic propagation. *J. Microsc.* **176**(2), 167–177 (1994)
29. Hautière, N., Aubert, D.: Contrast restoration of foggy images through use of an onboard camera. In: IEEE Conference on Intelligent Transportation Systems, Vienna, Austria, pp. 1090–1095 (2005)

Author Biographies

Nicolas Hautière received his M.S. degree in civil engineering from the National School of State Public Works (ENTPE), Lyon, France in 2002 and his M.S. and Ph.D. degrees in computer vision from the University Jean Monnet, Saint-Etienne, France, in 2002 and 2005, respectively. Since 2009, he has been a research leader at the Laboratory for Road Operation, Perception, Simulations and Simulators (LEPSIS), which is a recent research unit of the French Institute of Science and Technology for Transport, Development and Networks (IFSTTAR). His research interests cover the modeling of the meteorological phenomena reducing the highway visibility, the detection of visibility conditions and the estimation of the visibility range.

Jean-Philippe Tarel graduated from Ponts ParisTech, Paris, France (1991). He received his Ph.D. degree in applied mathematics from Paris IX-Dauphine University in 1996. He was with the Institut National de Recherche en Informatique et Automatique (INRIA) from 1991 to 1996 and from 2001 to 2003. From 1997 to 1998, he worked as a research associate at Brown University, USA. From 1999, he has been a researcher in the French Institute of Science and Technology for Transport, Development and Networks (IFSTTAR and formerly LCPC), Paris, France. His research interests include 3D reconstruction, pattern recognition and detection.

Houssam Halmaoui received his M.S. degree in machine vision in 2008 and an M.S. degree in electronics and signal processing from the University of Burgundy in 2009. He is currently a Ph.D. student at the LIVIC and LEPSIS, IFSTTAR. His work concerns the image visibility restoration under bad weather conditions such as rain and fog.

Roland Brémont is a researcher at the University Paris Est (France) since 1996. He obtained his engineering degree from the Ponts Paris-Tech in Paris in 1990 and his Ph.D. from Mines ParisTech in 1993 in the field of image processing. His current researches focus on human vision for road safety applications, including road lighting, driving simulation and computer graphics.

Didier Aubert received his M.S. and Ph.D. degrees, respectively, in 1985 and 1989 from the National Polytechnical Institute of Grenoble (INPG). From 1989 to 1990, he worked as a research scientist on the development of an automatic road following system for the NAVLAB at Carnegie Mellon University. From 1990 to 1994, he worked in the research department of a private company (ITMI). During this period, he was the project leader of several projects dealing with computer vision.

In 1995, he joined INRETS (French National Institute for Transportation and Safety Research). He is currently a senior researcher and director of LEPSIS. He works on road traffic monitoring, crowd monitoring, automated highway systems and driving assistance systems. He is an image processing expert for several companies and teaches in several universities and engineer schools.